

JGR Atmospheres

RESEARCH ARTICLE

10.1029/2024JD042222

Key Points:

- Atmospheric river detection tools are applied to climate model simulations incorporating insolation and greenhouse gas changes
- AR frequency changes due to orbital forcing and associated changing seasonality generally agree across algorithms in most regions
- AR frequency changes due to lower greenhouse gas concentrations agree in sign, but there is substantial disagreement in magnitude

Correspondence to:

W. D. Rush,
wrush@scu.edu

Citation:

Rush, W. D., Lora, J. M., Skinner, C. B., Menemenlis, S. A., Shields, C. A., Ullrich, P., et al. (2025). Atmospheric river detection under changing seasonality and mean-state climate: ARTMIP tier 2 paleoclimate experiments. *Journal of Geophysical Research: Atmospheres*, 130, e2024JD042222. <https://doi.org/10.1029/2024JD042222>

Received 21 AUG 2024

Accepted 17 DEC 2024

Author Contributions:

Conceptualization: W. D. Rush, J. M. Lora, C. B. Skinner, C. A. Shields, L. R. Leung, F. M. Ralph, J. J. Rutz, M. Wehner

Formal analysis: W. D. Rush

Funding acquisition: J. M. Lora, C. A. Shields

Investigation: W. D. Rush, J. M. Lora, C. B. Skinner, S. A. Menemenlis, C. A. Shields, P. Ullrich, T. A. O'Brien, S. Brands, B. Guan, K. S. Mattingly, E. McClenney, K. Nardi, A. Nellikkattil, A. M. Ramos, K. J. Reid, E. Shearer, R. Tomé, J. D. Wille

Methodology: W. D. Rush, J. M. Lora, C. B. Skinner, C. A. Shields

Project administration: J. M. Lora, C. A. Shields

Resources: J. M. Lora, C. B. Skinner, C. A. Shields, P. Ullrich, T. A. O'Brien, S. Brands, B. Guan, K. S. Mattingly, E. McClenney, K. Nardi, A. Nellikkattil, A. M. Ramos, K. J. Reid, E. Shearer, R. Tomé, J. D. Wille

Supervision: J. M. Lora, C. A. Shields

Atmospheric River Detection Under Changing Seasonality and Mean-State Climate: ARTMIP Tier 2 Paleoclimate Experiments

W. D. Rush¹ , J. M. Lora² , C. B. Skinner³ , S. A. Menemenlis^{2,4}, C. A. Shields⁵ , P. Ullrich^{6,7}, T. A. O'Brien^{8,9} , S. Brands¹⁰ , B. Guan^{11,12}, K. S. Mattingly¹³, E. McClenney⁷ , K. Nardi¹⁴ , A. Nellikkattil^{15,16} , A. M. Ramos¹⁷, K. J. Reid¹⁸, E. Shearer¹⁹ , R. Tomé²⁰ , J. D. Wille^{21,22} , L. R. Leung²³ , F. M. Ralph²⁴ , J. J. Rutz²⁴, M. Wehner⁹ , Z. Zhang²⁴ , M. Lu²⁵, and K. T. Quagrainie⁸

¹Department of Environmental Studies and Sciences, Santa Clara University, Santa Clara, CA, USA, ²Department of Earth and Planetary Sciences, Yale University, New Haven, CT, USA, ³Department of Environmental, Earth and Atmospheric Sciences, University of Massachusetts Lowell, Lowell, MA, USA, ⁴Program in Atmospheric and Oceanic Sciences, Princeton University, Princeton, NJ, USA, ⁵Climate and Global Dynamics Division, National Center for Atmospheric Research, Boulder, CO, USA, ⁶Lawrence Livermore National Laboratory, Livermore, CA, USA, ⁷Department of Land, Air and Water Resources, University of California, Davis, CA, USA, ⁸Department of Earth and Atmospheric Sciences, Indiana University, Bloomington, IN, USA, ⁹Climate and Ecosystem Sciences Division, Lawrence Berkeley National Laboratory, Berkeley, CA, USA, ¹⁰Instituto de Física de Cantabria (IFCA), CSIC-UC, Santander, Spain, ¹¹Joint Institute for Regional Earth System Science and Engineering, University of California, Los Angeles, CA, USA, ¹²Jet Propulsion Laboratory, California Institute of Technology, Pasadena, CA, USA, ¹³Space Science and Engineering Center, University of Wisconsin-Madison, Madison, WI, USA, ¹⁴Department of Meteorology and Atmospheric Science, The Pennsylvania State University, University Park, PA, USA, ¹⁵Center for Climate Physics, Institute for Basic Science (IBS), Busan, South Korea, ¹⁶Department of Climate System, Pusan National University, Busan, Republic of Korea, ¹⁷Institute of Meteorology and Climate Research Troposphere Research (IMKTRO), Karlsruhe Institute of Technology, Karlsruhe, Germany, ¹⁸ARC Centre of Excellence for 21st Century Weather, University of Melbourne, Parkville, VIC, Australia, ¹⁹Center for Hydrometeorology and Remote Sensing, University of California, Irvine, CA, USA, ²⁰Faculdade de Ciências, Instituto Dom Luiz, Universidade de Lisboa, Lisbon, Portugal, ²¹Institut des Géosciences de l'Environnement, CNRS/UGA/IRD/G-INP, Saint Martin d'Hères, France, ²²Institute for Atmospheric and Climate Science, ETH Zurich, Zurich, Switzerland, ²³Atmospheric, Climate, and Earth Sciences Division, Pacific Northwest National Laboratory, Richland, WA, USA, ²⁴Center for Western Weather and Water Extremes, Scripps Institution of Oceanography, University of California San Diego, San Diego, CA, USA, ²⁵Department of Civil and Environmental Engineering, The Hong Kong University of Science and Technology, Clear Water Bay, Kowloon, Hong Kong

Abstract Atmospheric rivers (ARs) are filamentary structures within the atmosphere that account for a substantial portion of poleward moisture transport and play an important role in Earth's hydroclimate. However, there is no one quantitative definition for what constitutes an atmospheric river, leading to uncertainty in quantifying how these systems respond to global change. This study seeks to better understand how different AR detection tools (ARDTs) respond to changes in climate states utilizing single-forcing climate model experiments under the aegis of the Atmospheric River Tracking Method Intercomparison Project (ARTMIP). We compare a simulation with an early Holocene orbital configuration and another with CO₂ levels of the Last Glacial Maximum to a preindustrial control simulation to test how the ARDTs respond to changes in seasonality and mean climate state, respectively. We find good agreement among the algorithms in the AR response to the changing orbital configuration, with a poleward shift in AR frequency that tracks seasonal poleward shifts in atmospheric water vapor and zonal winds. In the low CO₂ simulation, the algorithms generally agree on the sign of AR changes, but there is substantial spread in their magnitude, indicating that mean-state changes lead to larger uncertainty. This disagreement likely arises primarily from differences between algorithms in their thresholds for water vapor and its transport used for identifying ARs. These findings warrant caution in ARDT selection for paleoclimate and climate change studies in which there is a change to the mean climate state, as ARDT selection contributes substantial uncertainty in such cases.

Plain Language Summary Atmospheric rivers are filaments of moisture in the atmosphere that play an important role in precipitation, but there is no one agreed-upon method to define them. This study compares multiple definitions of atmospheric rivers in climate models that either change the timing and intensity of seasons by altering the orbit or make the planet colder by lowering CO₂ levels. We found that the various

Visualization: W. D. Rush

Writing – original draft: W. D. Rush

Writing – review & editing: W. D. Rush, J. M. Lora, S. A. Menemenlis, C. A. Shields, P. Ullrich, T. A. O'Brien, S. Brands, B. Guan, K. S. Mattingly, A. Nellikkattil, A. M. Ramos, K. J. Reid, E. Shearer, J. D. Wille, Z. Zhang, M. Lu, K. T. Quagrainie

definitions of atmospheric rivers tended to agree in the model in which the seasons changed, but there was substantial disagreement in the model of the colder planet. The most likely reason for this is the definitions are based on modern-day observations. While the climate for the model with the altered seasons was on average similar to the modern, the colder model was substantially different, particularly as it relates to the amount of water in the atmosphere.

1. Introduction

Atmospheric rivers (ARs) are an important component of global moisture transport. Despite making up only a small fraction of the area of the midlatitudes at any time, they account for a majority of the atmospheric poleward moisture transport (Ralph & Dettinger, 2011; Ralph et al., 2018; Zhu & Newell, 1998). They play a crucial role in regional hydroclimates worldwide and are likely to become increasingly significant as the climate continues to warm (Zhang et al., 2024), particularly for ARs on the west coasts of continents, including Europe, North and South America, Australia, East Asia, and high latitude regions such as Antarctica (Meneghini et al., 2007; Neiman et al., 2008; Pan & Lu, 2019, 2020; Pohl et al., 2021; Ralph et al., 2004; Reid et al., 2022; Viale & Nuñez, 2011; Wille et al., 2021). ARs are also often associated with extreme precipitation events that pose significant hazards such as flooding and landslides (Corringham et al., 2019; Huang et al., 2020; Lavers & Villarini, 2013; Ralph et al., 2006; Waliser & Guan, 2017).

ARs are highly variable phenomena that can be affected by a variety of forcings, including greenhouse gases and aerosols, which have warming and cooling influences on the global climate, respectively (Baek & Lora, 2021; Bellouin et al., 2020; Deser et al., 2020; Myhre et al., 2013). The impact of the variability of the annular modes on ARs alone can constitute regional precipitation variations on the scale of 20 mm per month (Baek et al., 2023). Previous studies on ARs in both past and future warmer worlds suggest an increase in the frequency and size of ARs and an increase in the intensity of the associated precipitation as a result of thermodynamic changes (Baek & Lora, 2021; Espinoza et al., 2018; Menemenlis et al., 2021; O'Brien et al., 2022; Payne et al., 2020; Shields et al., 2021, 2023; Skinner et al., 2023; Zhang et al., 2024). Paleoclimate studies also suggest that the distribution of AR activity and landfall locations is strongly influenced by dynamical changes, which are subject to changes in both the mean state and seasonality of the climate (Lora et al., 2017, 2023; Shields et al., 2021; Skinner et al., 2020).

There is no single agreed-upon quantitative definition as to what constitutes an AR (Ralph et al., 2017; Shields et al., 2018), which complicates comparisons between results across climate states and using different methodologies. The goal of the Atmospheric River Tracking Method Intercomparison Project (ARTMIP) is to understand and quantify the uncertainties associated with the various AR detection tools (ARDTs) that have been developed to identify ARs (Shields et al., 2018). This is important as the various metrics associated with ARs, such as their frequency, size, intensity, and location, can vary depending on the detection method used (Lora et al., 2020; O'Brien et al., 2022; Pan & Lu, 2019; Rutz et al., 2019; Shields et al., 2018). In future climates, ARDTs generally show increases in frequency and intensity of ARs, but the variation in magnitude of the predicted changes is more related to ARDT selection than model uncertainties (O'Brien et al., 2022; Shields et al., 2023). Due to the variability in the detection thresholds between different ARDTs, generally those with more stringent requirements detect fewer ARs than those with more lenient requirements (Rutz et al., 2019).

This study investigates AR frequency changes in single-forcing climate model experiments, in which only a single climate forcing is changed relative to the preindustrial climate. Here, we alter greenhouse gas concentrations and the Earth's orbit to assess whether uncertainties in resulting AR detections are sensitive to the character of climate change, that is, whether there is a robust difference that arises as a result of changes to the mean climate state versus changes to the seasonality and distribution of insolation. While previous studies have utilized the same base states across models (O'Brien et al., 2022), or the impacts of additional metrics such as shape and attributable precipitation in high-resolution models (Shields et al., 2018), this is the first ARTMIP study to incorporate the varying ARDT responses to orbital changes. As previous studies have shown that ARDT selection has a greater impact on AR frequency and intensity than model or reanalysis uncertainty, our study extends analysis of ARDT-associated uncertainty to different climate states even if there is no change to the mean state (Collow et al., 2022). This is particularly valuable for paleoclimate studies as forcings often combine, for

Table 1
CESM Forcing Parameters

Simulation	CO ₂	Solar forcing	Eccentricity	Obliquity	Precession
Preindustrial	284 ppm	1,365 Wm ⁻²	0.016724	23.446°	102.04°
10ka	284 ppm	1,365 Wm ⁻²	0.019419	24.227°	294.82°
Low CO ₂	190 ppm	1,365 Wm ⁻²	0.016724	23.446°	102.04°

example, when there are greenhouse gas-driven and orbitally driven changes occurring simultaneously (Lora et al., 2023; Oster et al., 2023; Shields et al., 2021; Skinner et al., 2020).

To that end, our paleoclimate simulations are based on two periods with extensive proxy and model characterization: the early Holocene and the Last Glacial Maximum (LGM). Correspondingly, we simulate an equilibrium climate state with altered orbital parameters appropriate for the early Holocene, hereafter referred to as the “10ka” simulation, and another with reduced greenhouse gas concentrations consistent with those from the LGM, hereafter referred to as the “low CO₂” simulation. As our experiments are single-forcing simulations, they are not direct reflections of either the early Holocene or the LGM. This is to say that the “10ka” simulation varies from the preindustrial only in its orbit, and the “low CO₂” varies only in its CO₂ levels, that is, there were no changes to the ice sheets relative to preindustrial. However, we are able to draw some parallels from the proxy characterizations of these time periods to guide our subsequent analyses.

During the early Holocene, CO₂ levels and global temperatures were roughly similar to the preindustrial (Mayewski et al., 2004). However, there were substantial differences in regional climates driven in large part by an altered seasonality associated with the changed orbital parameters, including increased temperatures in the high latitude North Atlantic, and a global reworking of the hydrologic cycle, with some regions wetter and others drier (Mayewski et al., 2004; Tierney & deMenocal, 2013; Zhang et al., 2020). A notable example is the African humid period and greening of the Sahara, which saw significant increases in precipitation over the Sahara and Sahel as evidenced in ocean sediment records, leaf wax isotopes, and lake records (Holmes & Hoelzmann, 2017; McGee et al., 2013; Tierney & deMenocal, 2013).

By contrast, the LGM was approximately 6°C colder than the preindustrial period in part as a result of much lower atmospheric greenhouse gas concentrations, although this was also amplified by large increases in ice sheets and the associated change in global albedo (which is absent in our simulation) (Schneider von Deimling et al., 2006). Thermodynamic scaling of the hydrologic cycle during the Last Glacial Maximum would broadly entail precipitation minus evaporation (P-E) decreases in the subtropics and increases in the tropics and high latitudes, but again, there were large regional exceptions (Boos, 2012; Lora, 2018). As an example, southwestern North America has been of particular interest as there is copious evidence of increased precipitation and large lakes in this region during the LGM (Amaya et al., 2022; Lofverstrom, 2020; Lora et al., 2017, 2023; Morrill et al., 2018; Oster et al., 2015). In short, the two simulations represent a change in seasonalities and a change in the mean states of the climate. The question we seek to answer is when moving to a different climate state, how do these differing changes impact the detection of ARs among the suite of ARDTs utilized.

2. Materials and Methods

2.1. Model Simulations

We use simulations with the Community Earth System Model version 1.2 (CESM1.2) (Hurrell et al., 2013). Our CESM configuration includes the Community Atmosphere Model version 5 (CAM5) (Neale et al., 2010), the Community Land Model version 4.5 (CLM4.5) (Fisher et al., 2015), the Community Ice Code version 4 (CICE4) (Bailey et al., 2011), and the Parallel Ocean Program version 2 (POP2) (Danabasoglu et al., 2012). The atmosphere and land models were run on a $0.9^\circ \times 1.25^\circ$ finite volume grid, while the ocean and sea ice models were run at a nominal 1° resolution. We produced three simulations: a preindustrial control simulation, a simulation with an early Holocene (10ka) orbital configuration (Table 1) that alters the seasonality of insolation without substantially changing the annual mean state (and is otherwise identical to the preindustrial case), and a simulation with low CO₂ configuration (same as preindustrial, but with 190 ppm CO₂) in which the mean climate cools relative to the control. The simulations were initialized from the same preindustrial state with an equilibrated ocean. The 10ka simulation was integrated for 200 years, followed by an additional 100-year analysis period. The low CO₂ simulation was spun up for 300 years followed by a 100-year analysis period. Equilibrium was determined via global average surface temperatures. All analyses were derived from 6-hourly climatological averages, with interpolations applied to correct for the calendar effect on the changing timing of seasons when relevant. The exact calendar date of the equinoxes/solstices will vary due to the changes in orbit. Therefore, to have a more direct comparison between simulations, time series analysis is plotted in solar longitude, the angular position of

the Earth along its orbital plane, rather than the day of a year; this ensures seasonal results are comparable. 0°L_s corresponds to the boreal vernal equinox, 90°L_s with the boreal summer solstice, 180°L_s with the boreal autumnal equinox, and 270°L_s with the boreal winter solstice (Bartlein et al., 2019; Chen et al., 2011). For the preindustrial and low CO_2 simulations, seasons as defined by JJA, SON, DJF, and MAM are defined by the days in which they coincide with the modern calendar. In making adjustments for the 10ka simulation, the start of each season was adjusted such that it coincided with the same solar longitude as the preindustrial rather than the calendar day.

2.2. ARTMIP Experimental Design and Catalogs

ARTMIP Tier 2 consists of sensitivity experiments, using a subset of AR detection algorithms from the Tier 1 experiments (Rutz et al., 2019; Shields et al., 2018) from participants who elected to take part in the next round of experiments investigating specific questions. To investigate the sensitivity of AR detection to changes in seasonality versus changes in the mean-state climate, participants in this Tier 2 ARTMIP experiment were provided with data from the final 30 years of each of our simulations described in Section 2.1 in order to create catalogs of AR detections, from which metrics can be directly compared. In total, 14 ARDTs were used in this experiment, although three participants provided multiple versions of their ARDTs. The ARDTs used in this study are listed in Table 2. AR detection criteria typically involve instantaneous integrated vapor transport (IVT) and/or integrated water vapor (IWV), and can be defined either using absolute thresholds, fixed relative thresholds which are held to a historical reference point, relative thresholds which utilize a time-varying reference, or some combination thereof. Several algorithms (Brands, IDL, and Reid) considered multiple thresholds and thus produced several AR catalogs each. The Brands methods were run with thresholds calculated from the preindustrial simulation, generally used as reference here, and additionally with thresholds from its respective “own” experiment, that is, 10ka and low CO_2 thresholds were used when analyzing the 10ka and low CO_2 experiment, respectively. For example, the 10ka simulation was tested using the thresholds calculated for the preindustrial simulation and the low CO_2 simulation in addition to its own thresholds, while the Reid algorithm utilized two absolute values for IVT. In the case of SCAFET, a precipitation threshold is also used. Additionally, ARDTs employ different geometric requirements to define the shape of the ARs. Finally, some algorithms are global, while some have been designed specifically for certain regions (Mattingly et al., 2018; O’Brien et al., 2021; Rutz et al., 2019; Wille et al., 2021).

We investigated AR detection results from the algorithms by analyzing the spatiotemporal changes in AR frequency as detected in each of the simulations. AR frequency for each algorithm was determined by taking the mean AR detection across all years for each algorithm. As the algorithms exhibited a nonnormal distribution of frequency, the median of these means was used to calculate the trend among the algorithms. For the purposes of calculating the median of all algorithms, the median value of each grouping from a specific algorithm was used so as to avoid biasing the ensemble toward a particular ARDT. The change in frequency of landfalling ARs along coastlines was analyzed relative to the preindustrial simulation. Regions of interest include Western Europe (38.16°N – 57.96°N), western North America (31.57°N – 55.13°N), and Chile (30.62°S – 55.13°S). Longitudes varied, but were manually fitted to coastlines, averaged over 1.25 – 3.75° depending on coastal morphology at a given latitude. AR-related precipitation was calculated by multiplying the binary AR detection for each ARDT for each timestep against the total precipitation at the corresponding timestep. For TECA-BARD, which generates probability fields for the presence of an atmospheric river, a threshold probability of 0.667 was used to determine the binary “likely” ARs. Regional ARDTs were excluded from transects for which they did not have coverage.

3. Results

3.1. Model Characterization

3.1.1. 10ka Orbit Model

Despite the fact that we utilize single-forcing simulations, as opposed to full paleoclimate simulations, we are able to draw parallels between our results and paleoclimate records. Previous studies of early Holocene climate show an increase in seasonality, particularly with higher temperatures at high latitudes in the Northern Hemisphere during boreal summer associated with the orbital configuration at the time (Jones & Yu, 2010; Zhang et al., 2022). Consistently, in our 10ka simulation, the change in orbital parameters results in more insolation reaching the surface during boreal summer in the Northern Hemisphere and less insolation reaching the Southern Hemisphere during austral summer, relative to preindustrial. These strong seasonality changes nevertheless occur without

Table 2

Description of the ARDT Algorithms Included in Analyses

Algorithm name	Geometry	Threshold	Region	Reference
AR-Connect v2	Object identification	700 kg m ⁻¹ s ⁻¹ (seeding) and 300 kg m ⁻¹ s ⁻¹ (growing) IVT	Global, latitudes >23.25°	Shearer et al., 2020
Brands ^a (1.1, 1.2, 2.1, 2.2, 3.1, 3.2)	>1,500 km length	IVT v1.1 and 1.2: 95th percentile and 250 kg m ⁻¹ s ⁻¹ at detection, 90th percentile and 250 kg m ⁻¹ s ⁻¹ along structure v2.1 and 2.2: 90th percentile and 500 kg m ⁻¹ s ⁻¹ at detection, 85th percentile and 250 kg m ⁻¹ s ⁻¹ along structure v3.1 and 3.2: 90th percentile and 250 kg m ⁻¹ s ⁻¹ at detection, 85th percentile and 250 kg m ⁻¹ s ⁻¹ along structure v ^a .1 uses preindustrial thresholds and v ^a .2 uses own thresholds of the respective simulation	150°W to 30°E 30°N to 62°N	Brands et al., 2017 and https://github.com/SwenBrands/AR_detector
Guan and Waliser v2	>2,000 km length; >2:1 length to width; coherent IVT direction within 45° of AR shape orientation and with poleward component	85th percentile IVT; 100 kg m ⁻¹ s ⁻¹ IVT	Global	Guan & Waliser, 2015
IDL ^a (PI, 10ka, 21ka)	>1,500 km length and latitudinal movement <4.5°N	85th percentile IVT	Western Europe and South Africa ^a	Ramos et al., 2016
IPART v1	>1,500 km length; area in range [50 ^a 10 ⁴ , 1,800 ^a 10 ⁴ km ²]; >2:1 length to width; isoperimetric quotient <0.7; and centroid latitude >20°N, <80°N.	Transient IVT plumes standing out from a temporal scale of 8 days	Northern Hemisphere	Xu et al., 2020
Lora v2	>2,000 km length	225 kg m ⁻¹ s ⁻¹ IVT above time/latitude dependent threshold from 30 days and zonal mean IWV	Global	Skinner et al., 2020
Mattingly v2	>1,500 km length; >1.5:1 length to width	85th percentile IVT relative to 31-day climatological mean; 150 m ⁻¹ s ⁻¹ IVT; and poleward vIVT if at <66.56° N/S	Global, latitudes >10°	Mattingly et al., 2018
Mundhenk v3	>1,400 km length and aspect ratio 1:4	Temporal and spatial IVT percentiles/anomalies	Global, latitudes >15°	Mundhenk et al., 2016
Reid ^a (250, 500)	>2,000 km length; >2:1 length to width; and orientation angle >10°	250 kg m ⁻¹ s ⁻¹ or 500 kg m ⁻¹ s ⁻¹ IVT	Global	Reid et al., 2020
SCAFET v1		Precipitation >1 mm day ⁻¹	Global	Nellikkattil et al., 2024
Shields v1	>2:1 length to width	Zonal mean moisture; regional 85th percentile wind; and 850-mb wind magnitudes	Western U.S. Iberian Peninsula, UK; landfalling only	Shields & Kiehl, 2016a, 2016b
teca_bard v1.0.1	Area dependent upon percentile threshold exceeded	Spatial percentile with inverted Gaussian filter applied at the equator	Global	O'Brien et al., 2020
TEMPEST (TE v2.1)	Cluster size minimum = 40,000 km ²	8-point Laplacian of IVT at distance 10° < -20000 kg m ⁻² s ⁻¹ deg ⁻²	Global, latitudes >15°	Ullrich & Zarzycki, 2021, https://github.com/ClimateGlobalChange/tempestextremes
Wille v2	>20° (2,000 km) length	98th percentile IWV or vIVT based on monthly climatological means	Polar: Antarctic (37.5°–78°S; Arctic (37.5°–80°N)	Wille et al., 2021

^aIndicates multiple iterations of algorithm applied.

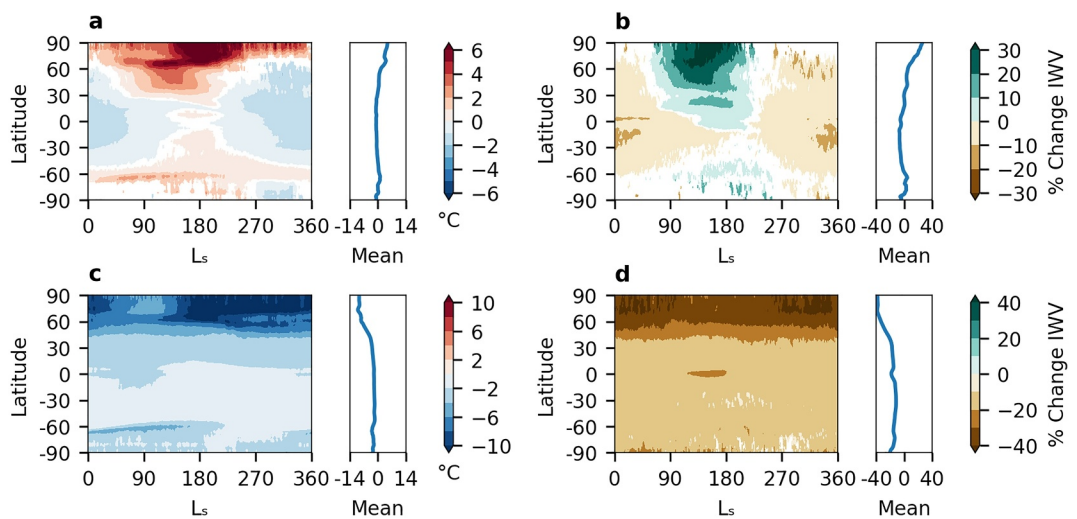


Figure 1. Annual cycle changes in temperature (a), (c) and integrated water vapor (b), (d) between the 10ka simulation (a), (b) and the low CO₂ simulations (c), (d) relative to preindustrial. Values plotted relative to solar longitude (L_s), that is, the angular position of the Earth along its orbital plane. 0°L_s corresponds to the boreal vernal equinox, 90°L_s with the boreal summer solstice, 180°L_s with the boreal autumnal equinox, and 270°L_s with the boreal winter solstice. Only significant changes ($p < 0.01$) are shown. Note differing scales between the 10ka and low CO₂ comparisons.

altering the annual average insolation, such that the simulation represents a scenario with a largely (but not entirely, due to, for example, hemispheric differences in geography) unaltered global mean-state climate. For context, while the low CO₂ simulation sees a decrease of 20.41% in global IWV and an average global temperature decrease of 3°C, the 10ka simulation sees an increase in global IWV of 2.56% and a negligible temperature decrease.

The increase in boreal summer insolation results in higher temperatures in the Northern Hemisphere at high latitudes ($>60^{\circ}\text{N}$), as well as a greater seasonal change in temperature and IWV at midlatitudes to high-latitudes in the Northern Hemisphere (30–60°N) (Figure 1a). Higher temperatures and IWV in the Northern Hemisphere start during boreal summer and extend until the autumnal equinox, with generally drier and cooler conditions elsewhere throughout the year (Figures 1a and 1b). Additionally, the seasonal changes to IWV demonstrate marked latitudinal shifts. These poleward shifts are associated with the increased insolation driving higher temperatures, which in turn leads to the increase in IWV. The Southern Hemisphere experiences modestly warmer temperatures year-round at 60°S, and an enhanced seasonality in temperature changes between the equator and 60°S (Figure 1a). Changes in IWV concentrations are less pronounced than in the Northern Hemisphere; nevertheless, the Southern Hemisphere experiences a significant increase in IWV seasonally centered at 60°S. This increase begins in late austral winter, concomitant with the Northern Hemisphere's summertime changes, and carries through until the summer solstice (Figure 1b).

Wind patterns also demonstrate significant shifts in response to the changes in orbit. The most robust signals occur during JJA in the midlatitudes to high-latitudes in the North Pacific, wherein higher surface pressure in much of the basin results in an anticyclonic anomaly leading to enhanced flow impacting the Bering Strait region (Figure 2c). There is also a significant change during JJA in the pressure gradient over equatorial Africa, leading to a significant, robust increase in 850 hPa zonal wind strength toward the African continent from the Atlantic (Figure 2c). In the Southern Hemisphere, during SON, there is a significant increase in the pressure gradient between midlatitudes and high-latitudes in the southern Pacific resulting in a similar increase in anticyclonic winds, at 60°S, as in the North Pacific (Figure 2d). IVT demonstrates a robust increase in JJA in the North Pacific off the coast of Alaska as well as a concurrent, robust increase over the African continent, and off the eastern coast of North America (Figure 3c). Likewise, there is a decrease in moisture transport into the South Pacific Convergence Zone (SPCZ) resulting in localized drying, particularly in JJA and SON (Figures 3c and 3d).

These combined changes in moisture content and wind patterns result in a shift in global precipitation patterns (Figure 4). There is an 8.09% increase in global precipitation; however, these increases are primarily focused on

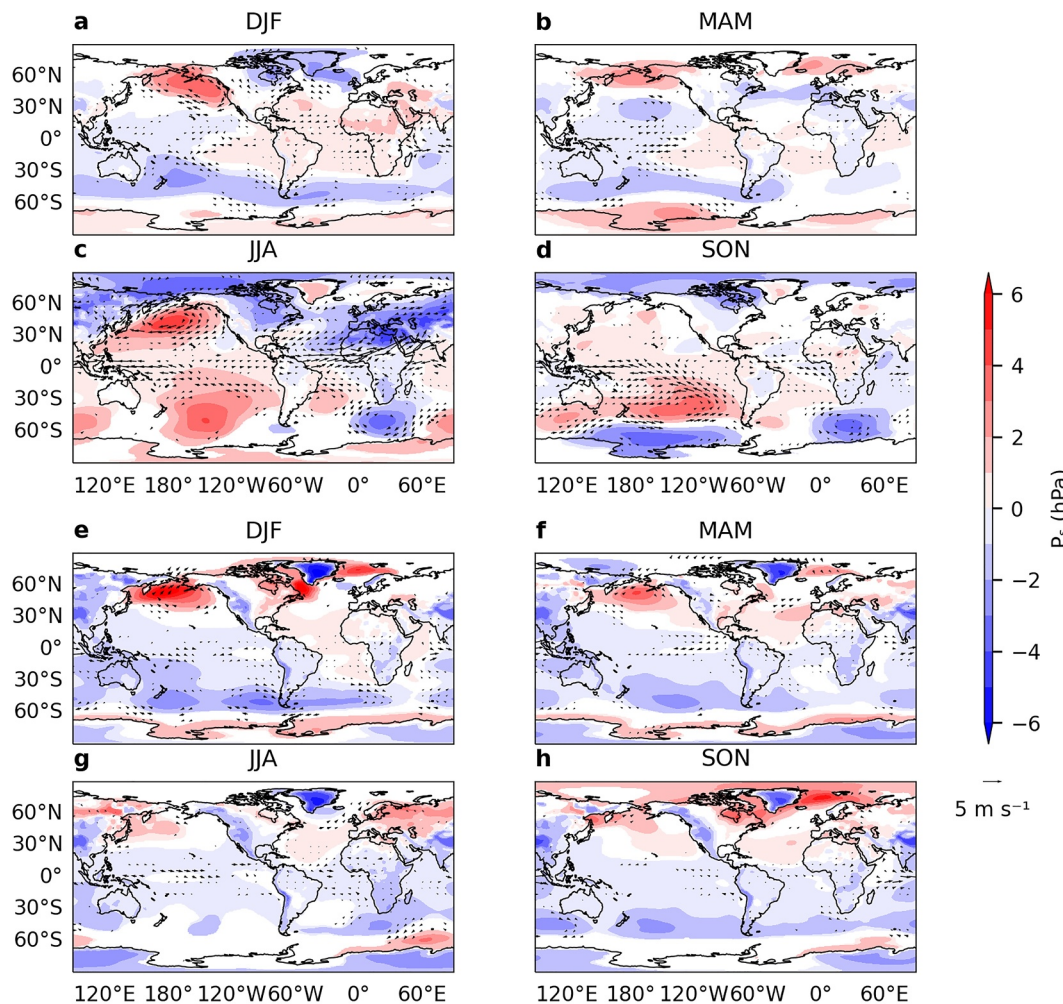


Figure 2. Seasonal changes (as defined by solar longitude) in surface pressure and 850 hPa winds in the 10ka (a–d) and low CO₂ simulations (e–h) relative to preindustrial. For surface pressure, values with $p < 0.01$ are shown, and for 850 hPa winds, values with $p < 0.05$ are shown.

tropical regions, that is, the Sahara/Sahel regions of Africa, the Arabian Peninsula, and the Indian subcontinent (Figures 3c and 3d). Excluding the tropics where ARs do not occur, at latitudes greater than 30°, precipitation increases by only 1.72%.

On the whole, the 10ka simulation results in a change in distribution of precipitation, both temporally and spatially, relative to the preindustrial. For example, DJF exhibits a decrease in precipitation at the equator in the Pacific and in sub-Saharan Africa, but this is accompanied by the aforementioned increase in tropical precipitation north and south of the equator as well as over the Atlantic and Indian Oceans in the tropics (Figure 4a). In regions relevant to ARs, JJA precipitation shows an increase at high latitudes in the Pacific and a decrease in the midlatitudes, mirroring trends seen in wind, surface pressure, and water vapor, that is, precipitation changes correspond to the sign of changes in IVT (Figure 4c). These precipitation pattern changes, particularly in the Sahara/Sahel, are consistent with proxy records of the early Holocene (Holmes & Hoelzmann, 2017; McGee et al., 2013; Tierney & deMenocal, 2013).

3.1.2. Low CO₂ Model

Previous studies of LGM climate suggest a cooler world, consistent with lower CO₂ levels (e.g., Annan & Hargreaves, 2013; Tierney & deMenocal, 2013). Global mean precipitation is lower in a cooler climate, consistent with the Clausius-Clapeyron relation and global energy budget constraints on the hydrologic cycle

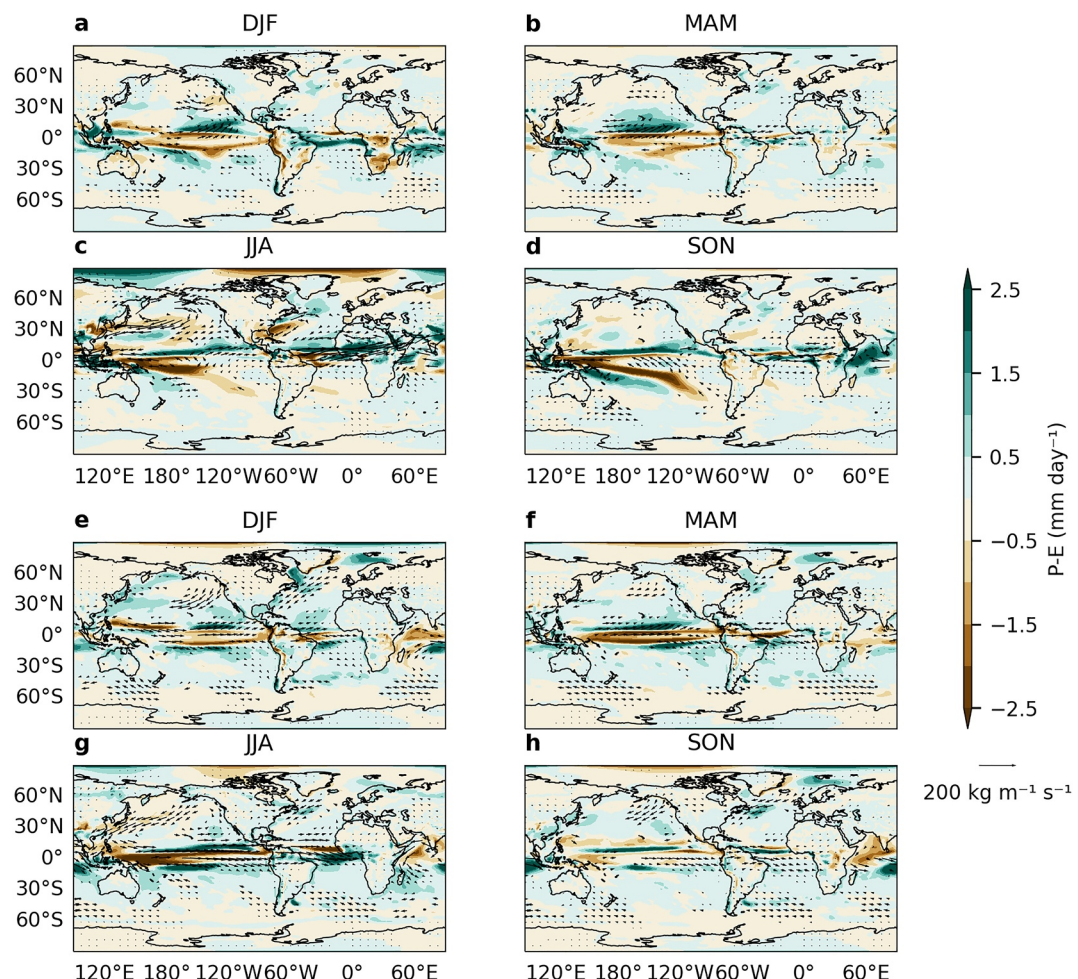


Figure 3. Seasonal changes (as defined by solar longitude) in integrated vapor transport (IVT, arrows) and precipitation minus evaporation (P-E, colors) changes in the 10ka simulation (a–d) and low CO_2 (e–h) relative to preindustrial. Insignificant changes ($p \geq 0.05$) are masked out.

(Allen & Ingram, 2002; Held & Soden, 2006). Decreases in tropospheric humidity also imply decreases in P-E in the tropics and high latitudes, and increases in P-E in the subtropics (Held & Soden, 2006). There are a number of studies that suggest localized increases in precipitation, particularly at western boundary sites (Begin et al., 2016; Goldsmith et al., 2017; Kirby et al., 2013; Oster et al., 2015; Tabor et al., 2021). These changes are often attributed to the LGM ice sheets resulting in changes in topography and albedo, which in turn result in changes in mechanical steering of atmospheric circulation and changes in air-sea interaction (Amaya et al., 2022; COHMAP Members, 1988; Lora, 2018; Lora et al., 2017; Lora et al., 2023; Manabe & Broccoli, 1985; Oster et al., 2015; Tabor et al., 2021). Lacking the ice sheet changes, our low CO_2 simulations broadly suggest a cooler, drier world, with significantly lower temperatures relative to preindustrial occurring at all latitudes but particularly enhanced at high latitudes in the Northern Hemisphere, due to polar amplification (Figures 1c and 1d) (Cohen et al., 2014). In contrast to the 10ka simulation, these changes represent a substantial mean-state change to the climate, but one largely controlled by thermodynamic changes. Consequently, IWV is also significantly lower at all latitudes, with the largest relative changes occurring at high latitudes in the northern hemisphere (Figure 1d).

Compared to the changes observed in the 10ka simulation relative to the preindustrial, there is relatively little change in the 850 hPa wind strength or direction in the low CO_2 simulation (Figures 2e–2h). There is a shift in equator-to-pole pressure gradients, with an increase in surface pressure at high latitudes in the Northern Hemisphere during SON and DJF and a decrease in pressure at lower latitudes, although these responses are also less pronounced (Figures 2e–2h).

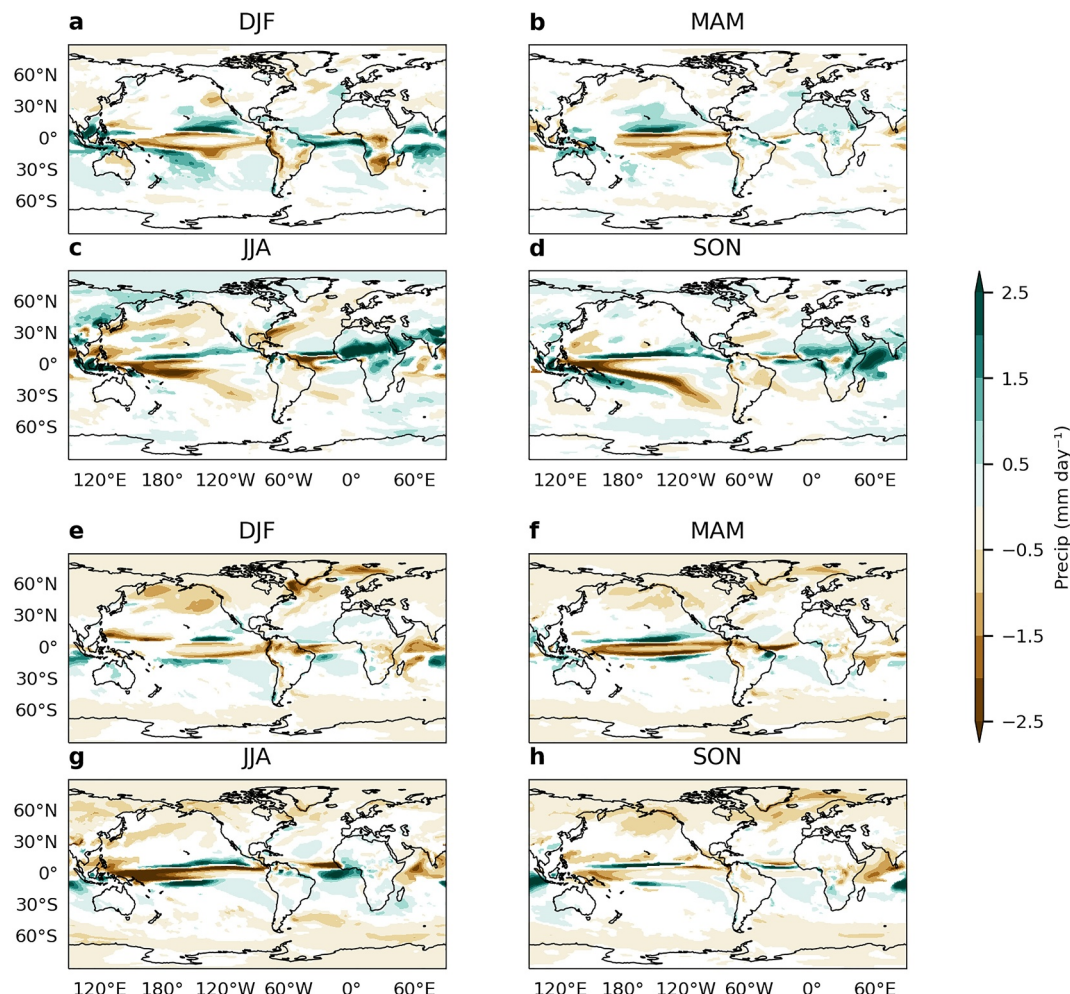


Figure 4. Seasonal changes (as defined by solar longitude) in precipitation in the 10ka simulation (a–d) and low CO₂ (e–h) relative to preindustrial. Insignificant changes ($p \geq 0.01$) are masked out. Of particular note are latitudinal poleward shifts in JJA in the northern Atlantic and northern Pacific, and in SON in the southern Pacific. Note the general extratropical precipitation decrease in the low CO₂ simulation, particularly at high latitudes.

There is also a global decrease in poleward moisture transport at subtropical and extratropical latitudes at all seasons (Figures 3e–3h). Consequently, the P-E reflects a decrease in evaporation rates at midlatitudes and an associated decrease in precipitation elsewhere, largely reflecting thermodynamic decreases, consistent with the expectation from Held & Soden, 2006 (Figures 3e–3h).

Precipitation patterns in the low CO₂ simulation follow the trends seen in I WV, that is, there is a pronounced, significant decrease in global precipitation of 7.28% (Figures 4e–4h). Although some regions see increases, primarily around the ITCZ, the changes observed in this simulation show a stark contrast to those observed in the 10ka simulation, in that they represent not only a reworking of the distribution, but a general decrease in precipitation, evaporation, and moisture transport.

3.2. ARDT Responses to Changing Climate States

The changes in global moisture transport result in a substantial reworking of AR distribution and frequencies as detected by our suite of ARDTs. In the 10ka simulation, there is a latitudinal shift in the median AR frequency, with a decrease in AR frequency at lower latitudes. The largest magnitude of change in AR frequency occurs in the North Pacific and is marked by a general poleward shift (Figure 5a). The South Pacific contains a similar poleward shift in AR frequency, although of a smaller magnitude. In the North Atlantic, there are changes in AR frequency of a smaller magnitude which occur off the East Coast of the United States and the Iberian Peninsula

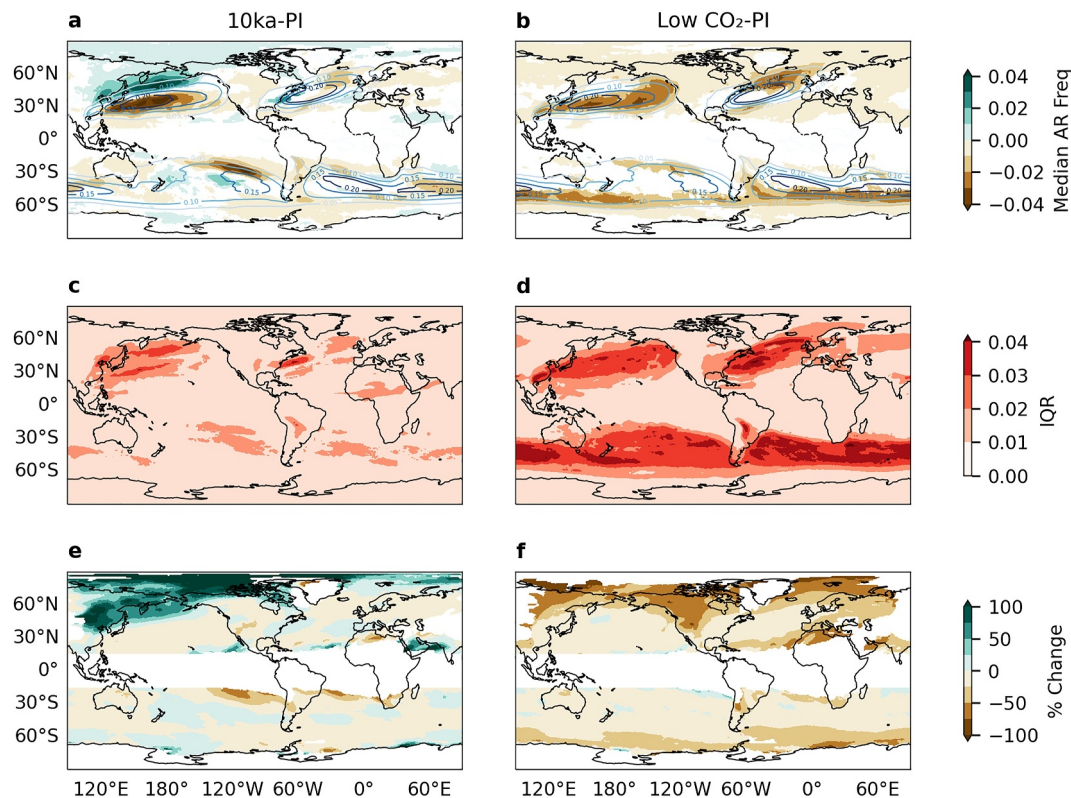


Figure 5. Changes in mean AR frequencies taken across medians of all algorithms in 10ka simulation (a) and low CO₂ simulation (b) relative to preindustrial. Median of ARDTs for preindustrial indicated by contours in (a) and (b). Note general latitudinal shifts in AR detection (a) and general decrease in AR detection (b). These changes are consistent with changes in IWV, wind speed, and moisture transport (Figures 1, 2, and 4). (c) Interquartile range (IQR) of mean AR frequency across ARDTs in the 10ka simulation relative to the preindustrial (c) and low CO₂ simulation relative to the preindustrial (d). Note greater spread in frequency across ARDTs in the low CO₂ simulation. Percentage change in median AR detection in the 10ka simulation relative to the preindustrial (e) and low CO₂ simulation relative to the preindustrial (f). Note increase in AR detection at high latitudes in Northern Hemisphere in 10ka simulation (e), and general decrease in AR activity in low CO₂ simulation (f).

(Figure 5a). However, rather than a latitudinal shift, these changes coincide with a decrease over the Atlantic Basin and a corresponding increase at the margins, and a significant increase in AR frequency in the Northern Hemisphere from approximately 45–75°N between solar longitudes (L_s) 90–180°, corresponding to boreal summer (Figure 6a). These high latitude shifts result in an increase in AR frequency in excess of 100% at high latitudes (Figure 5e). There is also a statistically significant, although smaller magnitude, shift in the Southern Hemisphere between 35 and 65°S centered around 180° L_s , that is, austral vernal equinox. These Southern Hemisphere increases in AR frequency are on the order of 50% higher than preindustrial values (Figure 5e). In total, however, global median AR frequency is only about 1.45% above its preindustrial value.

As expected, these changes in the ARDTs correspond clearly to the trends observed in IWV, IVT, and winds. The latitudinal shifts in median AR frequency are closely related to the increases in water vapor at high latitudes in the Northern Hemisphere during boreal summer and in the Southern Hemisphere surrounding the austral vernal equinox (Figure 1b). The changing pressure gradients resulting in altered atmospheric circulation over the North Pacific and North Atlantic during JJA and the South Pacific during SON are in line with the regions which experienced increased AR frequency (Figures 2c and 2d). The confluence of these increases in moisture and wind speed results in altered IVT in these regions, leading to the shifts in AR frequency (Figures 4c and 4d).

For the low CO₂ simulation, there is a significant, near-global decrease in AR frequency (Figures 5b and 6b). The greatest decreases are seen between 30 and 60° in each hemisphere, principally around the cores of the preindustrial AR tracks. That is, the decreases largely indicate width contractions of the AR tracks accompanied by

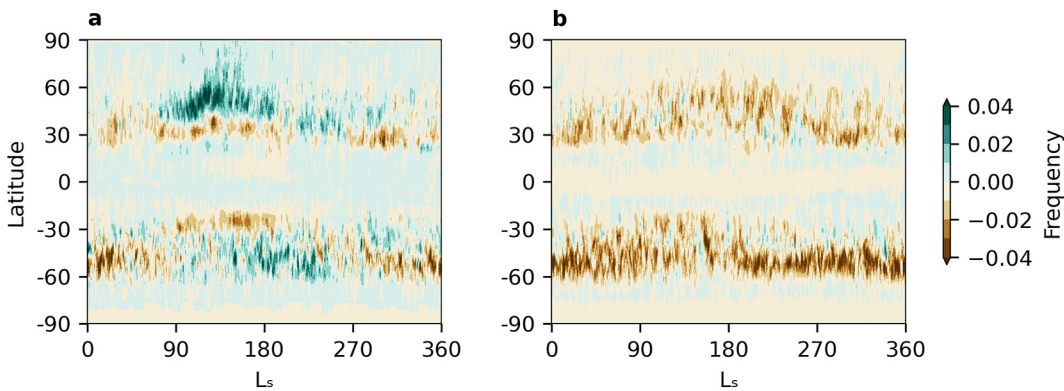


Figure 6. Median annual cycle AR frequency (wherein 1 would indicate a constant state of AR detection) in 10ka (a) and low CO₂ (b) simulations relative to preindustrial. Values plotted relative to solar longitude (L_s), that is, the angular position of the Earth along its orbital plane. 0°L_s corresponds to the boreal vernal equinox, 90°L_s with the boreal summer solstice, 180°L_s with the boreal autumnal equinox, and 270°L_s with the boreal winter solstice. In 10ka simulation (a), note latitudinal shifts in AR activity beginning in boreal summer in both hemispheres. In 21ka model (b), note general decrease in AR activity.

equatorward shifts in the Southern Hemisphere and North Atlantic (specifically, the decrease in AR frequency is larger on the poleward flanks of these tracks); in the North Pacific, the signal suggests an overall decrease in AR frequency. Global median AR frequency in the low CO₂ simulation is 22.2% below its preindustrial value, with the largest decreases occurring at high latitudes in the Northern Hemisphere, on the order of 80%–90% (Figure 5f). Compared to the 10ka simulation, there is no shift in the timing of the decreases in AR counts, and the decreases are generally distributed evenly throughout the year (Figure 6). As discussed above, this is consistent with the characterization of the low CO₂ simulation, which exhibits a decrease in global mean precipitation, evaporation, and moisture transport (Figures 1d, 3e–3h and 4e–4h).

In both simulations, changes in AR-related precipitation are strongly linked to the changes in AR frequency. In the 10ka simulation, there is a marked increase in AR-related precipitation at high latitudes in the North Pacific, coincident with a decrease in AR-related precipitation at lower latitudes and consistent with a poleward shift (Figure 7a). Likewise, there is also a decrease in AR-related precipitation in the central North Atlantic as well as an increase near the Iberian Peninsula. AR-related precipitation also decreases in the southern Pacific, coincident with the decrease in AR frequency in the same region. In the low CO₂ simulation, AR-related precipitation decreases in the core of the AR tracks, coincident with the decrease in AR frequency (Figure 7b).

In looking at the impacts of ARs along coastlines in regions with high AR activity, the 10ka simulation shows an increase in AR activity in southern Europe (approximately 25%), with relatively little change at higher latitudes (Figure 8a). In western North America, there is a decrease in AR activity at lower latitudes (approximately 25%) and a slight increase at higher latitudes (Figure 8c). Along the Chilean coast, there is a decrease at higher latitudes (approximately 40%) with little change elsewhere (Figure 8e). The low CO₂ simulation generally shows a decrease in AR activity along all of these regions. However, there is a substantial spread among the ARDTs (Figures 8b–8d and 8f).

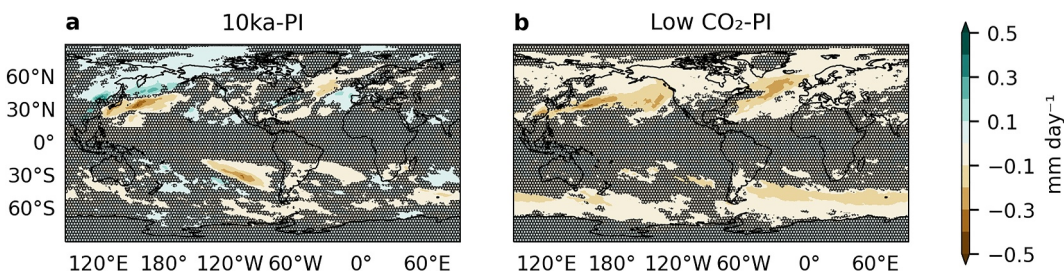


Figure 7. Changes in AR-related precipitation in the 10ka simulation (a) and low CO₂ simulation (b) relative to preindustrial. Stippling indicates where fewer than 90% of ARDTs agree on change in sign.

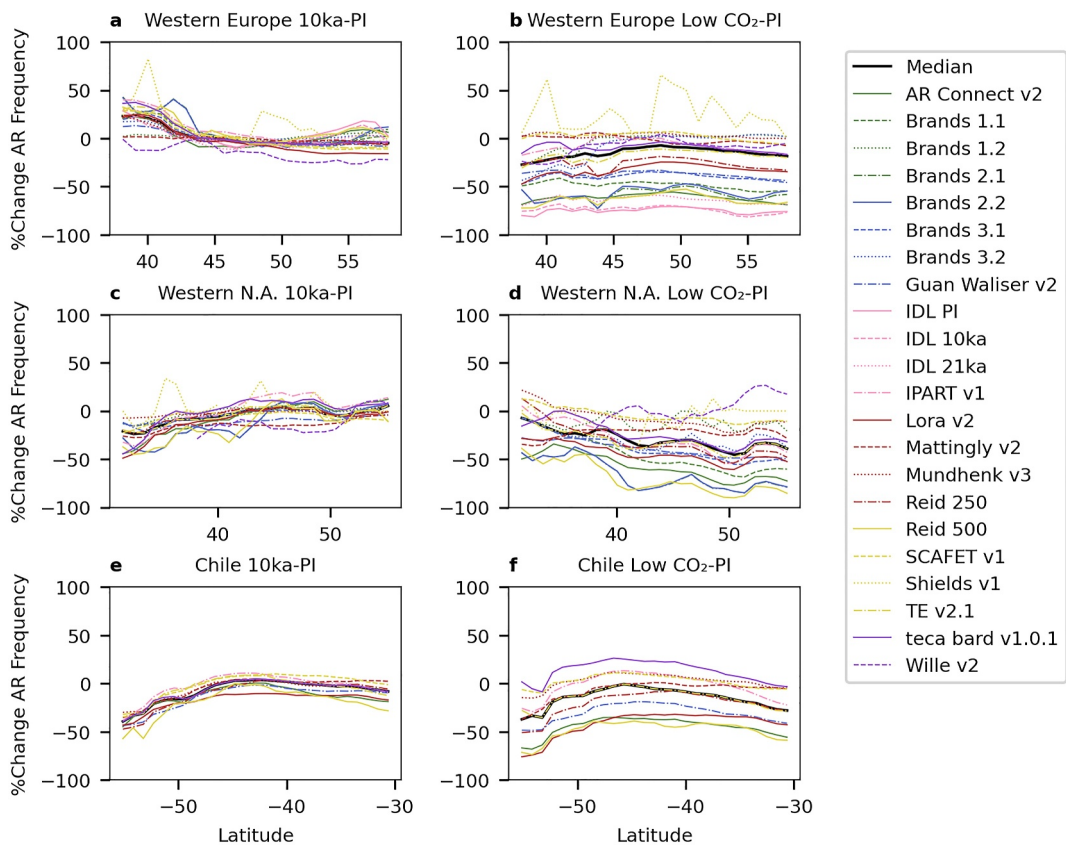


Figure 8. Changes in mean relative AR frequency along coastline transects between 10ka and preindustrial (a), (c), and (e) and low CO₂ and preindustrial (b), (d), and (f) for individual algorithms in Western Europe (a), (b), western North America (c), (d), and Chile (e), (f). Median of algorithm means represented by a thick black line. Note decreased spread among algorithms in the 10ka model compared to the low CO₂ model. Regional ARDTs are excluded from subplots in which they do not have coverage.

To characterize the spread among the ARDTs in response to the changing climate states, we analyzed the interquartile range, or IQR, of the distribution of changes from each ARDT between the preindustrial and the 10ka/low CO₂ simulations. A larger IQR corresponds with a greater spread in the distribution of values in the magnitude of change, and thus lower agreement, among the ARDTs. In all cases, the ARDTs demonstrate a lower IQR, and therefore a smaller spread (and greater agreement) in the changes between the 10ka and preindustrial simulations relative to the changes between the low CO₂ and preindustrial simulations (Figures 5c and 5d).

Although there is a clear global change among the algorithms in the low CO₂ simulation relative to the preindustrial, there is substantial disagreement as to the magnitude of that change (Figure 5d). While both the 10ka and low CO₂ simulations result in changes in AR distribution and frequency, the spread of values associated with individual ARDTs is much greater in the low CO₂ simulation than in the 10ka simulation (Figure 5c, 5d, 8).

This is to say, despite variable detection sensitivity between ARDTs (i.e., more sensitive ARDTs detect more ARs than less sensitive ARDTs), the relative change in AR frequency between ARDTs is remarkably consistent when comparing the 10ka simulation to the preindustrial (Figure 8a). In other words, ARDTs that utilize lower detection thresholds (e.g., lower IVT requirements) detect more ARs than ARDTs with higher detection thresholds (e.g., higher IVT requirements). However, these high or low detection frequencies are consistent between the 10ka and the preindustrial simulations, that is, those that detected a high number of ARs continued to do so, and at approximately the same rate between the simulations, hence the resulting relatively minor changes in relative AR occurrence (save for a consistent latitudinal shift among algorithms) and a narrow range around the median.

However, the spread among the ARDTs even in terms of relative changes is substantially larger in the low CO₂ simulation (Figure 8b). This is to say that algorithms with high or low detection frequencies in the preindustrial

simulation were not consistent in their detection frequency in the low CO₂ simulation, resulting in a larger spread in the relative changes between algorithms. For instance, ARDTs with absolute IVT requirements tuned to present conditions may find those requirements consistently met in the preindustrial simulation, but IVT may approach the defined threshold less frequently in the low CO₂ simulation. Likewise, ARDTs that rely upon reaching a percentile threshold of IVT relative to the given atmospheric state may find a more consistent detection rate as IVT will always be at the defined percentile somewhere on the planet. Other tuning parameters, such as only detecting landfalling ARs or tuning to a specific latitudinal range, likely also play a role in determining detection frequency.

4. Discussion

The change in the orbital configuration of the 10ka simulation resulted in a rearrangement of the spatiotemporal distribution of temperature, surface pressure, water vapor, and wind speed. However, these changes did not drastically change the mean state of the climate relative to the preindustrial. In contrast, the low CO₂ simulation showed significant changes to the mean climate state, with a reduction in temperatures and moisture transport occurring nearly globally. This is relevant within the context of AR detection as many algorithms are designed for, and in some cases specifically tuned to, the modern climate state.

Despite the relative complexity of the shifts in AR distributions in the 10ka simulation, agreement among the algorithms in the areas that experienced changes in moisture content/transport is generally high (Figures 1a–1c, 3a–3d, 5a, 5c, 8a, 8c and 8e). However, while the sign of change among the algorithms in the low CO₂ simulation is generally consistent, and consistent with the overall thermodynamic expectation in a globally cooled climate, the magnitude of that change is not (Figures 1b–1d, 3e–3h, 5b, 5d, 8b, 8d and 8f). Although the ARDTs vary in their usage of relative or absolute thresholds and the sensitivity of those thresholds, the suite of ARDTs utilized in this study is consistent in their detection between the 10ka simulation and the preindustrial. In other words, an ARDT with a low sensitivity in the preindustrial remains insensitive in the 10ka simulation. Between the different ARDTs, the magnitude of relative change is comparable even amongst those with higher or lower sensitivities to AR detection. However, in comparing ARDTs between the preindustrial and the low CO₂ simulation, even by looking at relative changes to account for algorithms that have higher or lower sensitivities, there is a substantial spread in the degree of the relative changes.

This disagreement likely arises from how thresholds are defined among the various ARDTs. While an algorithm tuned to an absolute threshold of IVT may be consistent when there is no mean change in the climate state, as in the preindustrial versus the 10ka simulation, these absolute thresholds will experience a different exceedance frequency in a different mean-state climate. For example, a warmer world with a higher moisture content in the atmosphere will exceed a given threshold more frequently than a cooler world with a lower moisture content, suggesting ARDTs that utilize relative thresholds may be more applicable across a greater range of climate states.

This is of utmost importance when conducting analyses of AR activity under different climate states. Previous studies on ARs in future climate states have shown similarly that, under ongoing climate change incorporating global warming, the greatest uncertainties in future AR size, frequency, and intensity result not from model uncertainty, but from disagreement among ARDTs (O'Brien et al., 2021; Shields et al., 2023). Here, we arrive at similar findings in that there is notable uncertainty that arises from ARDT selection in the low CO₂ simulations while there is considerably less spread resulting from the change in orbit, indicating that how ARDTs handle the mean background climate in their detections of ARs is the principal source of disagreement, and should be considered carefully in future studies. This indicates that, in paleoclimate studies wherein there are generally changes in orbit as well as changes in other forcings, the forcings that principally alter the mean state will lead to the greatest spread among ARDTs, and therefore, care must be taken in ARDT selection for analyses of such altered climates, when there is substantial change to the water vapor content of the atmosphere. Nevertheless, it is also worth noting that the qualitative agreement between ARDTs even in our low CO₂ simulation suggests that ARs had a considerable role in shaping past climate change.

The disagreement between ARDTs in altered climate states touches on the philosophical question underlying ARTMIP and how exactly we define an AR. If an AR is viewed by its geometrical definition of being a narrow filament of moisture transport, it may be more appropriate to utilize relative thresholds for IVT given the changing

Acknowledgments

This work was funded in part by NSF Awards AGS-1903528, AGS-1903600, and EAR-2102853. ARTMIP is a grassroots community effort and includes a collection of international researchers from universities, laboratories, and agencies. ARTMIP has received support from the US Department of Energy Office of Science Biological and Environmental Research (BER) as part of the Regional and Global Climate Modeling program, and the Center for Western Weather and Water Extremes (CW3E) at Scripps Institute for Oceanography at the University of California, San Diego. CAS was supported by the Regional and Global Model Analysis (RGMA) component of the Earth and Environmental System Modeling Program of the U.S. Department of Energy's Office of Biological and Environmental Research (BER) under Award Number DE-SC0022070 and the National Center for Atmospheric Research, which is a major facility sponsored by the National Science Foundation (NSF) under Cooperative Agreement No. 1852977. KJR was supported by the Australian Research Council Centre of Excellence for Climate Extremes (CE170100023) and the National Computational Infrastructure (NCI Australia). Work performed by PAU is under the auspices of the DOE by Lawrence Livermore National Laboratory under Contract DE-AC52-07NA27344. LRL is supported by DOE Office of Science Biological and Environmental Research as part of the Water Cycle and Climate Extremes Modeling (WACCEM) scientific focus area funded by the Regional and Global Model Analysis program area. PNNL is operated for DOE by Battelle Memorial Institute under contract DE-AC05-76RL01830. The effort of TAO and KTQ was supported by the Environmental Resilience Institute, funded by Indiana University's Prepared for Environmental Change Grand Challenge initiative, in part by Lilly Endowment, Inc., through its support for the Indiana University Pervasive Technology Institute and in part by the U.S. Department of Energy, Office of Science, Office of Biological and Environmental Research, Climate and Environmental Sciences Division, and Regional and Global Model Analysis Program under Contract Number DE-AC02-05CH11231 and under award number DE-SC0023519. BG was supported by NASA Grants 80NSSC20K1344, 80NSSC21K1007, and 80NSSC22K0926, and the California Department of Water Resources. AMR was supported by the Helmholtz 'Changing Earth' program. KSM was supported by the Polar Radiant Energy in the Far Infrared Experiment (PREFIRE) mission, NASA Grant 80NSSC18K1485. J.D.W. acknowledges support from the French Agence Nationale de la Recherche projects ANR-20-CE01-0013 (ARCA).

climate states. However, if it is defined, for example, as a region with $>250 \text{ kg m}^{-1} \text{ s}^{-1}$ of moisture transport, the absolute thresholds may be more appropriate. Further, in the latter instance where moisture transport is at question rather than the form that moisture transport takes, it may be most appropriate to utilize IVT directly under altered climate states. Another complicating factor in utilizing relative thresholds is that similar moisture transport does not necessarily correspond to similar impacts in altered climates. As an example, a state in which moisture transport events are similar but the static stability of the atmosphere is altered could lead to differences in AR precipitation despite identified ARs behaving similarly. Although ARDTs represent attempts to objectively quantify ARs, each of them is ultimately a qualitative judgment made by its author and design choices are linked to specific questions or applications. While some ARDTs may fall above or below the median value in terms of changes to relative detection frequencies, this does not necessarily mean that these ARDTs are "wrong", as the median of a set of quantitative values derived from qualitative assessments is not more physically meaningful than the individual values. This is to say, in selecting an ARDT for a particular application, the selection should be dependent on the question being considered. What is perhaps most salient is that a collection of ARDTs, as presented here, offers a quantification of the uncertainty associated with AR detection.

5. Conclusions

In this paper, we have tested a suite of algorithms for the detection of ARs in two climate simulations under a single-forcing change relative to preindustrial: one in which the orbit was set to a 10ka configuration, and one in which CO₂ levels were set to those of the LGM. These simulations can be interpreted as providing a change in seasonality versus a change in the mean state of the climate, with which we can test the sensitivity of ARDTs to these two cases. For the 10ka simulation, most algorithms indicated a change in the distribution and timing of ARs that generally corresponded to changes in IWV and IVT, mainly associated with intensified boreal summer. Despite the complexity of the spatiotemporal shifts in the 10ka simulation, there was good agreement among the algorithms in the magnitude of changes in most regions. On the other hand, while the algorithms generally agreed on an overall decrease in AR activity linked to an overall cooler climate in the low CO₂ configuration, there was substantial disagreement in the magnitude of that change. This disagreement likely arises from how the different algorithms prescribe thresholds for IWV or IVT. These findings strongly suggest that (some) ARDTs may be overtuned to present-day conditions, and may therefore not be directly applicable across all climate states or immediately intercomparable. As a result, care is warranted in selecting ARDTs that consider the background mean state of the atmosphere when applying AR detection to studies of paleoclimate and climate change.

Conflict of Interest

The authors declare no conflicts of interest relevant to this study.

Data Availability Statement

Details on catalogs are found on the ARTMIP website, <https://www.cgd.ucar.edu/projects/artmip>, and all data are on Rutz et al. (2024). Data can be downloaded from <https://rda.ucar.edu/datasets/d651019/> and <https://doi.org/10.5065/MTDW-0V06>.

References

- Allen, M. R., & Ingram, W. J. (2002). Constraints on future changes in climate and the hydrologic cycle. *Nature*, 419(6903), 224–232. <https://doi.org/10.1038/nature01092>
- Amaya, D. J., Seltzer, A. M., Karnauskas, K. B., Lora, J. M., Zhang, X., & DiNezio, P. N. (2022). Air-sea coupling shapes North American hydroclimate response to ice sheets during the Last Glacial Maximum. *Earth and Planetary Science Letters*, 578, 117271. <https://doi.org/10.1016/j.epsl.2021.117271>
- Annan, J. D., & Hargreaves, J. C. (2013). A new global reconstruction of temperature changes at the Last Glacial Maximum. *Climate of the Past*, 9(1), 367–376. <https://doi.org/10.5194/cp-9-367-2013>
- Baek, S. H., Battaglio, J. M., & Lora, J. M. (2023). Atmospheric river variability over the last millennium driven by annular modes. *AGU Advances*, 4(1), e2022AV000834. <https://doi.org/10.1029/2022AV000834>
- Baek, S. H., & Lora, J. M. (2021). Counterbalancing influences of aerosols and greenhouse gases on atmospheric rivers. *Nature Climate Change*, 11(11), 958–965. <https://doi.org/10.1038/s41558-021-01235-y>
- Bailey, D., Holland, M., Hunke, E., Lipscomb, B., Briegleb, B., Bitz, C., & Schramm, J. (2011). Community ice Code (CICE) user's guide version 4.0 released with CCSM 4.0. *Tech rep, Los Alamos National Library*.
- Bartlein, P. J., & Shafer, S. L. (2019). Paleo calendar-effect adjustments in time-slice and transient climate-model simulations (PaleoCalAdjust v1.0): Impact and strategies for data analysis. *Geoscientific Model Development*, 12(9), 3889–3913. <https://doi.org/10.5194/gmd-12-3889-2019>

- Beghin, P., Charbit, S., Kageyama, M., Combourieu-Nebut, N., Hatté, C., Dumas, C., & Peterschmitt, J.-Y. (2016). What drives LGM precipitation over the western Mediterranean? A study focused on the Iberian Peninsula and northern Morocco. *Climate Dynamics*, 46(7–8), 2611–2631. <https://doi.org/10.1007/s00382-015-2720-0>
- Bellouin, N., Quaas, J., Gryspeert, E., Kinne, S., Stier, P., Watson-Parris, D., et al. (2020). Bounding global aerosol radiative forcing of climate change. *Reviews of Geophysics*, 58(1), e2019RG000660. <https://doi.org/10.1029/2019RG000660>
- Boos, W. R. (2012). Thermodynamic scaling of the hydrological cycle of the last glacial maximum. *Journal of Climate*, 25(3), 992–1006. <https://doi.org/10.1175/jcli-d-11-00010.1>
- Brands, S., Gutiérrez, J. M., & San-Martín, D. (2017). Twentieth-century atmospheric river activity along the west coasts of Europe and North America: Algorithm formulation, reanalysis uncertainty and links to atmospheric circulation patterns. *Climate Dynamics*, 48(9–10), 2771–2795. <https://doi.org/10.1007/s00382-016-3095-6>
- Chen, G. S., Kutzbach, J. E., Gallimore, R., & Liu, Z. (2011). Calendar effect on phase study in paleoclimate transient simulation with orbital forcing. *Climate Dynamics*, 37(9–10), 1949–1960. <https://doi.org/10.1007/s00382-010-0944-6>
- Cohen, J., Screen, J. A., Furtado, J. C., Barlow, M., Whittleston, D., Coumou, D., et al. (2014). Recent Arctic amplification and extreme mid-latitude weather. *Nature Geoscience*, 7(9), 627–637. <https://doi.org/10.1038/ngeo2234>
- Cohmap, M. (1988). Climatic changes of the last 18,000 years: Observations and model simulations. *Science*, 241(4869), 1043–1052. <https://doi.org/10.1126/science.241.4869.1043>
- Collow, A. B., Shields, C. A., Guan, B., Kim, S., Lora, J. M., McClenney, E. E., et al. (2022). An overview of ARTMIP's tier 2 reanalysis intercomparison: Uncertainty in the detection of atmospheric rivers and their associated precipitation. *Journal of Geophysical Research-Atmosphere*, 127(8). <https://doi.org/10.1029/2021JD036155>
- Corringham, T. W., Ralph, F. M., Gershunov, A., Cayan, D. R., & Talbot, C. A. (2019). Atmospheric rivers drive flood damages in the western United States. *Science Advances*, 5(12), eaax4631. <https://doi.org/10.1126/sciadv.aax4631>
- Danabasoglu, G., Bates, S. C., Briegleb, B. P., Jayne, S. R., Jochum, M., Large, W. G., et al. (2012). The CCSM4 ocean component. *Journal of Climate*, 25(5), 1361–1389. <https://doi.org/10.1175/JCLI-D-11-00091.1>
- Deser, C., Phillips, A. S., Simpson, I. R., Rosenbloom, N., Coleman, D., Lehner, F., et al. (2020). Isolating the evolving contributions of anthropogenic aerosols and greenhouse gases: A new CESM1 large ensemble community resource. *Journal of Climate*, 33(18), 7835–7858. <https://doi.org/10.1175/JCLI-D-20-0123.1>
- Espinosa, V., Waliser, D. E., Guan, B., Lavers, D. A., & Ralph, F. M. (2018). Global analysis of climate change projection effects on atmospheric rivers. *Geophysical Research Letters*, 45(9), 4299–4308. <https://doi.org/10.1029/2017GL076968>
- Fisher, R. A., Muszala, S., Vertenstein, M., Lawrence, P., Xu, C., McDowell, N. G., et al. (2015). Taking off the training wheels: The properties of a dynamic vegetation model without climate envelopes, CLM4.5. *Geoscientific Model Development*, 8(11), 3593–3619. <https://doi.org/10.5194/gmd-8-3593-2015>
- Goldsmith, Y., Polissar, P., Ayalon, A., Bar-Matthews, M., Demenocal, P., & Broecker, W. S. (2017). The modern and Last Glacial Maximum hydrological cycles of the Eastern Mediterranean and the Levant from a water isotope perspective. *Earth and Planetary Science Letters*, 457, 303–312. <https://doi.org/10.1016/j.epsl.2016.10.017>
- Guan, B., & Waliser, D. E. (2015). Detection of atmospheric rivers: Evaluation and application of an algorithm for global studies. *Journal of Geophysical Research: Atmospheres*, 120(24), 12514–12535. <https://doi.org/10.1002/2015JD024257>
- Guan, B., Waliser, D. E., & Ralph, F. M. (2018). An intercomparison between reanalysis and dropsonde observations of the total water vapor transport in individual atmospheric rivers. *Journal of Hydrometeorology*, 19(2), 321–337. <https://doi.org/10.1175/JHM-D-17-0114.1>
- Held, I. M., & Soden, B. J. (2006). Robust responses of the hydrological cycle to global warming. *Journal of Climate*, 19(21), 5686–5699. <https://doi.org/10.1175/JCLI3990.1>
- Holmes, J. A., & Hoelzmann, P. (2017). *Late pleistocene-holocene African Humid Period as evident in lakes*. Oxford University Press. <https://doi.org/10.1093/acrefore/9780190228620.013.531>
- Huang, X., Swain, D. L., & Hall, A. D. (2020). Future precipitation increase from very high resolution ensemble downscaling of extreme atmospheric river storms in California. *Science Advances*, 6(29), eaaba1323. <https://doi.org/10.1126/sciadv.aba1323>
- Hurrell, J. W., Holland, M. M., Gent, P. R., Ghan, S., Kay, J. E., Kushner, P. J., et al. (2013). The community earth system model: A framework for collaborative research. *Bulletin of the American Meteorological Society*, 94(9), 1339–1360. <https://doi.org/10.1175/BAMS-D-12-00121.1>
- Jones, M. C., & Yu, Z. (2010). Rapid deglacial and early Holocene expansion of peatlands in Alaska. *Proceedings of the National Academy of Sciences*, 107(16), 7347–7352. <https://doi.org/10.1073/pnas.0911387107>
- Kirby, M. E., Seaford, S. J., Bonuso, N., Fantozzi, J. M., & Hiner, C. A. (2013). Latest pleistocene to Holocene hydroclimates from lake Elsinore, California. *Quaternary Science Reviews*, 76, 1–15. <https://doi.org/10.1016/j.quascirev.2013.05.023>
- Lavers, D. A., & Villarini, G. (2013). Atmospheric rivers and flooding over the central United States. *Journal of Climate*, 26(20), 7829–7836. <https://doi.org/10.1175/JCLI-D-13-00212.1>
- Lofverstrom, M. (2020). A dynamic link between high-intensity precipitation events in southwestern North America and Europe at the Last Glacial Maximum. *Earth and Planetary Science Letters*, 534, 116081. <https://doi.org/10.1016/j.epsl.2020.116081>
- Lora, J. M. (2018). Components and mechanisms of hydrologic cycle changes over north America at the last glacial maximum. *Journal of Climate*, 31(17), 7035–7051. <https://doi.org/10.1175/JCLI-D-17-0544.1>
- Lora, J. M., Mitchell, J. L., Risi, C., & Tripati, A. E. (2017). North Pacific atmospheric rivers and their influence on western North America at the last glacial maximum. *Geophysical Research Letters*, 44(2), 1051–1059. <https://doi.org/10.1002/2016GL071541>
- Lora, J. M., Shields, C. A., & Rutz, J. J. (2020). Consensus and disagreement in atmospheric river detection: ARTMIP global catalogues. *Geophysical Research Letters*, 47(20), e2020GL089302. <https://doi.org/10.1029/2020GL089302>
- Lora, J. M., Skinner, C. B., Rush, W. D., & Baek, S. H. (2023). The hydrologic cycle and atmospheric rivers in CESM2 simulations of the Last Glacial Maximum. *Geophysical Research Letters*, 50(18), e2023GL104805. <https://doi.org/10.1029/2023GL104805>
- Manabe, S., & Broccoli, A. J. (1985). The influence of continental ice sheets on the climate of an ice age. *Journal of Geophysical Research*, 90(D1), 2167–2190. <https://doi.org/10.1029/JD090iD01p02167>
- Mattingly, K. S., Mote, T. L., & Fettweis, X. (2018). Atmospheric river impacts on Greenland Ice Sheet surface mass balance. *Journal of Geophysical Research: Atmospheres*, 123(16), 8538–8560. <https://doi.org/10.1029/2018JD028714>
- Mayewski, P. A., Rohling, E. E., Stager, J. C., Karlén, W., Maasch, K. A., Meeker, L. D., et al. (2004). Holocene climate variability. *Quaternary Research*, 62(3), 243–255. <https://doi.org/10.1016/j.yqres.2004.07.001>
- McGee, D., de Menocal, P. B., Winckler, G., Stuut, J. B. W., & Bradtmiller, L. I. (2013). The magnitude, timing and abruptness of changes in North African dust deposition over the last 20,000 yr. *Earth and Planetary Science Letters*, 371, 163–176. <https://doi.org/10.1016/j.epsl.2013.12.043>

- Meneghini, B., Simmonds, I., & Smith, I. N. (2007). Association between Australian rainfall and the southern annular mode. *International Journal of Climatology: A Journal of the Royal Meteorological Society*, 27(1), 109–121. <https://doi.org/10.1002/joc.1370>
- Menemenlis, S., Lora, J. M., Lofverstrom, M., & Chandan, D. (2021). Influence of stationary waves on mid-Pliocene atmospheric rivers and hydroclimate. *Global and Planetary Change*, 204, 103557. <https://doi.org/10.1016/j.gloplacha.2021.103557>
- Morrill, C., Lowry, D. P., & Hoell, A. (2018). Thermodynamic and dynamic causes of pluvial conditions during the Last Glacial Maximum in western North America. *Geophysical Research Letters*, 45(1), 335–345. <https://doi.org/10.1002/2017GL075807>
- Mundhenk, B. D., Barnes, E. A., & Maloney, E. D. (2016). All-season climatology and variability of atmospheric river frequencies over the North Pacific. *Journal of Climate*, 29(13), 4885–4903. <https://doi.org/10.1175/JCLI-D-15-0655.1>
- Myhre, G., et al. (2013). In T. F. Stocker (Ed.), *Climate change 2013: The physical science basis*. IPCC, Cambridge Univ. Press.
- Neale, R. B., Chen, C. C., Gettelman, A., Lauritzen, P. H., Park, S., Williamson, D. L., et al. (2010). Description of the NCAR community atmosphere model (CAM5.0). *NCAR Tech. Rep. NCAR/TN-486+STR*, 268.
- Neiman, P. J., Ralph, F. M., Wick, G. A., Lundquist, J. D., & Dettinger, M. D. (2008). Meteorological characteristics and overland precipitation impacts of atmospheric rivers affecting the West Coast of North America based on eight years of SSM/I satellite observations. *Journal of Hydrometeorology*, 9(1), 22–47. <https://doi.org/10.1175/2007JHM855.1>
- Nellikkattil, A. B., Lemmon, D., O'Brien, T. A., Lee, J. Y., & Chu, J. E. (2024). Scalable feature extraction and tracking (SCAFET): A general framework for feature extraction from large climate data sets. *Geoscientific Model Development*, 17(1), 301–320. <https://doi.org/10.5194/gmd-17-301-2024>
- O'Brien, T. A., Risser, M. D., Loring, B., Elbashandy, A. A., Krishnan, H., Johnson, J., et al. (2020). Detection of atmospheric rivers with inline uncertainty quantification: TECA-BARD v1. 0.1. *Geoscientific Model Development*, 13(12), 6131–6148. <https://doi.org/10.5194/gmd-13-6131-2020>
- O'Brien, T. A., Wehner, M. F., Payne, A. E., Shields, C. A., Rutz, J. J., Leung, L. R., et al. (2022). Increases in future AR count and size: Overview of the ARTMIP Tier 2 CMIP5/6 experiment. *Journal of Geophysical Research: Atmospheres*, 127(6), e2021JD036013. <https://doi.org/10.1029/2021JD036013>
- Oster, J. L., Ibarra, D. E., Winnick, M. J., & Maher, K. (2015). Steering of westerly storms over Western North America at the last glacial maximum. *Nature Geoscience*, 8(3), 201–205. <https://doi.org/10.1038/ngeo2365>
- Oster, J. L., Macarewicz, S., Lofverstrom, M., de Wet, C., Montañez, I., Lora, J. M., et al. (2023). North Atlantic meltwater during Heinrich Stadial 1 drives wetter climate with more atmospheric rivers in western North America. *Science Advances*, 9(46), eadj2225. <https://doi.org/10.1126/sciadv.adj2225>
- Pan, M., & Lu, M. (2019). A novel Atmospheric River identification algorithm. *Water Resources Research*, 55(7), 6069–6087. <https://doi.org/10.1029/2018WR024407>
- Pan, M., & Lu, M. (2020). East Asia Atmospheric River catalog: Annual cycle, transition mechanism and precipitation. *Geophysical Research Letters*, 47(15), e2020GL089477. <https://doi.org/10.1029/2020GL089477>
- Payne, A. E., Demory, M. E., Leung, L. R., Ramos, A. M., Shields, C. A., Rutz, J. J., et al. (2020). Responses and impacts of atmospheric rivers to climate change. *Nature Reviews Earth and Environment*, 1(3), 143–157. <https://doi.org/10.1038/s43017-020-0030-5>
- Pohl, B., Favier, V., Wille, J., Udy, D. G., Vance, T. R., Pergaud, J., et al. (2021). Relationship between weather regimes and atmospheric rivers in East Antarctica. *Journal of Geophysical Research: Atmospheres*, 126(24), e2021JD035294. <https://doi.org/10.1029/2021JD035294>
- Ralph, F. M., Dettinger, M., Lavers, D., Gorodetskaya, I. V., Martin, A., Viale, M., et al. (2017). Atmospheric rivers emerge as a global science and applications focus. *Bulletin of the American Meteorological Society*, 98(9), 1969–1973. <https://doi.org/10.1175/BAMS-D-16-0262.1>
- Ralph, F. M., & Dettinger, M. D. (2011). Storms, floods, and the science of atmospheric rivers. *Eos, Transactions American Geophysical Union*, 92(32), 265–266. <https://doi.org/10.1029/2011EO320001>
- Ralph, F. M., Dettinger, M. D., Cairns, M. M., Galarneau, T. J., & Eylander, J. (2018). Defining “atmospheric river”: How the Glossary of Meteorology helped resolve a debate. *Bulletin of the American Meteorological Society*, 99(4), 837–839. <https://doi.org/10.1175/BAMS-D-17-0157.1>
- Ralph, F. M., Neiman, P. J., & Wick, G. A. (2004). Satellite and CALJET aircraft observations of atmospheric rivers over the eastern North Pacific Ocean during the winter of 1997/98. *Monthly Weather Review*, 132(7), 1721–1745. [https://doi.org/10.1175/1520-0493\(2004\)132<1721:SACAOO>2.0.CO;2](https://doi.org/10.1175/1520-0493(2004)132<1721:SACAOO>2.0.CO;2)
- Ralph, F. M., Neiman, P. J., Wick, G. A., Gutman, S. I., Dettinger, M. D., Cayan, D. R., & White, A. B. (2006). Flooding on California's Russian River: Role of atmospheric rivers. *Geophysical Research Letters*, 33(13). <https://doi.org/10.1029/2006GL026689>
- Ramos, A. M., Nieto, R., Tomé, R., Gimeno, L., Trigo, R. M., Liberato, M. L., & Lavers, D. A. (2016). Atmospheric rivers moisture sources from a Lagrangian perspective. *Earth System Dynamics*, 7(2), 371–384. <https://doi.org/10.5194/esd-7-371-2016>
- Reid, K. J., King, A. D., Lane, T. P., & Hudson, D. (2022). Tropical, subtropical, and extratropical atmospheric rivers in the Australian region. *Journal of Climate*, 35(9), 2697–2708. <https://doi.org/10.1175/JCLI-D-21-0606.1>
- Reid, K. J., King, A. D., Lane, T. P., & Short, E. (2020). The sensitivity of atmospheric river identification to integrated water vapor transport threshold, resolution, and regridding method. *Journal of Geophysical Research: Atmospheres*, 125(20), e2020JD032897. <https://doi.org/10.1029/2020JD032897>
- Rutz, J. J., Shields, C. A., Lora, J. M., Payne, A. E., Guan, B., Ullrich, P., et al. (2019). The atmospheric river tracking method intercomparison project (ARTMIP): Quantifying uncertainties in atmospheric river climatology. *Journal of Geophysical Research: Atmospheres*, 124(24), 13777–13802. <https://doi.org/10.1029/2019JD030936>
- Rutz, J. J. C. A., et al. (2024). Atmospheric River tracking method intercomparison project tier 1 source data and catalogues. *Research Data Archive at the National Center for Atmospheric Research, Computational and Information Systems Laboratory*. <https://doi.org/10.5065/D62R3QFS>
- Schneider von Deimling, T., Ganopolski, A., Held, H., & Rahmstorf, S. (2006). How cold was the last glacial maximum? *Geophysical Research Letters*, 33(14). <https://doi.org/10.1029/2006GL026484>
- Shearer, E. J., Nguyen, P., Sellars, S. L., Analui, B., Kawzenuk, B., Hsu, K. L., & Sorooshian, S. (2020). Examination of global midlatitude atmospheric river lifecycles using an object-oriented methodology. *Journal of Geophysical Research: Atmospheres*, 125(22), e2020JD033425. <https://doi.org/10.1029/2020JD033425>
- Shields, C. A., & Kiehl, J. T. (2016a). Simulating the pineapple express in the half degree community climate system model, CCSM4. *Geophysical Research Letters*, 43(14), 7767–7773. <https://doi.org/10.1002/2016GL069476>
- Shields, C. A., & Kiehl, J. T. (2016b). Atmospheric river landfall-latitude changes in future climate simulations. *Geophysical Research Letters*, 43(16), 8775–8782. <https://doi.org/10.1002/2016GL070470>

- Shields, C. A., Kiehl, J. T., Rush, W., Rothstein, M., & Snyder, M. A. (2021). Atmospheric rivers in high-resolution simulations of the paleocene eocene thermal maximum (PETM). *Palaeogeography, Palaeoclimatology, Palaeoecology*, 567, 110293. <https://doi.org/10.1016/j.palaeo.2021.110293>
- Shields, C. A., Payne, A. E., Shearer, E. J., Wehner, M. F., O'Brien, T. A., Rutz, J. J., et al. (2023). Future atmospheric rivers and impacts on precipitation: Overview of the ARTMIP tier 2 high-resolution global warming experiment. *Geophysical Research Letters*, 50(6), e2022GL102091. <https://doi.org/10.1029/2022GL102091>
- Shields, C. A., Rutz, J. J., Leung, L. Y., Ralph, F. M., Wehner, M., Kawzenuk, B., et al. (2018). Atmospheric river tracking method intercomparison project (ARTMIP): Project goals and experimental design. *Geoscientific Model Development*, 11(6), 2455–2474. <https://doi.org/10.5194/gmd-11-2455-2018>
- Skinner, C. B., Lora, J. M., Payne, A. E., & Poulsen, C. J. (2020). Atmospheric river changes shaped mid-latitude hydroclimate since the mid-Holocene. *Earth and Planetary Science Letters*, 541, 116293. <https://doi.org/10.1016/j.epsl.2020.116293>
- Skinner, C. B., Lora, J. M., Tabor, C., & Zhu, J. (2023). Atmospheric river contributions to ice sheet hydroclimate at the last glacial maximum. *Geophysical Research Letters*, 50(1), e2022GL101750. <https://doi.org/10.1029/2022GL101750>
- Tabor, C., Lofverstrom, M., Oster, J., Wortham, B., de Wet, C., Montañez, I., et al. (2021). A mechanistic understanding of oxygen isotopic changes in the Western United States at the Last Glacial Maximum. *Quaternary Science Reviews*, 274, 107255. <https://doi.org/10.1016/j.quascirev.2021.107255>
- Tierney, J. E., & de Menocal, P. B. (2013). Abrupt shifts in Horn of Africa hydroclimate since the last glacial maximum. *Science*, 342(6160), 843–846. <https://doi.org/10.1126/science.1240411>
- Ullrich, P. A., Zarzycki, C. M., McClenney, E. E., Pinheiro, M. C., Stansfield, A. M., & Reed, K. A. (2021). TempestExtremes v2. 1: A community framework for feature detection, tracking, and analysis in large datasets. *Geoscientific Model Development*, 14(8), 5023–5048. <https://doi.org/10.5194/gmd-14-5023-2021>
- Viale, M., & Nuñez, M. N. (2011). Climatology of winter orographic precipitation over the subtropical central Andes and associated synoptic and regional characteristics. *Journal of Hydrometeorology*, 12(4), 481–507. <https://doi.org/10.1175/2010JHM1284.1>
- Waliser, D., & Guan, B. (2017). Extreme winds and precipitation during landfall of atmospheric rivers. *Nature Geoscience*, 10(3), 179–183. <https://doi.org/10.1038/ngeo2894>
- Wille, J. D., Favier, V., Gorodetskaya, I. V., Agosta, C., Kittel, C., Beeman, J. C., et al. (2021). Antarctic atmospheric river climatology and precipitation impacts. *Journal of Geophysical Research: Atmospheres*, 126(8), e2020JD033788. <https://doi.org/10.1029/2020JD033788>
- Xu, G., Ma, X., Chang, P., & Wang, L. (2020). Image-processing-based atmospheric river tracking method version 1 (IPART-1). *Geoscientific Model Development*, 13(10), 4639–4662. <https://doi.org/10.5194/gmd-13-4639-2020>
- Zhang, L., Zhao, Y., Cheng, T. F., & Lu, M. (2024). Future changes in global atmospheric rivers by CMIP6. *Journal of Geophysical Research: Atmospheres*, 129(3). <https://doi.org/10.1029/2023JD039359>
- Zhang, W., Wu, H., Cheng, J., Geng, J., Li, Q., Sun, Y., et al. (2022). Holocene seasonal temperature evolution and spatial variability over the Northern Hemisphere landmass. *Nature Communications*, 13(1), 5334. <https://doi.org/10.1038/s41467-022-33107-0>
- Zhang, Y., Renssen, H., Seppä, H., Valdes, P. J., & Li, J. (2020). Spatial contrasts of the Holocene hydroclimate trend between North and East Asia. *Quaternary Science Reviews*, 227, 106036. <https://doi.org/10.1016/j.quascirev.2019.106036>
- Zhu, Y., & Newell, R. E. (1998). A proposed algorithm for moisture fluxes from atmospheric rivers. *Monthly Weather Review*, 126(3), 725–735. [https://doi.org/10.1175/1520-0493\(1998\)126<0725:APAFMF>2.0.CO;2](https://doi.org/10.1175/1520-0493(1998)126<0725:APAFMF>2.0.CO;2)